

Synthesis, characterisation and water-gas shift activity of nano-particulate mixed-metal (Al, Ti) cobalt oxides

Moritz Wolf,^{a,b,1} Stephen J. Roberts,^a Wijnand Marquart,^{a,b} Ezra J. Olivier,^c Niels T. J. Luchters,^a Emma K. Gibson,^{d,e} C. Richard A. Catlow,^{d,f} Jan. H. Neethling,^c Nico Fischer,^{a,b} and Michael Claeys^{a,b,*}

^aCatalysis Institute, Department of Chemical Engineering, University of Cape Town, Private Bag X3, Rondebosch 7701, South Africa.

^bDST-NRF Centre of Excellence in Catalysis c*change, Private Bag X3, Rondebosch 7701, South Africa.

^cCentre for High Resolution Transmission Electron Microscopy, Physics Department, Nelson Mandela University, PO Box 77000, Port Elizabeth, 6031, South Africa.

^dUK Catalysis Hub, Research Complex at Harwell, RAL, Oxford, OX11 0FA, United Kingdom.

^eSchool of Chemistry, University of Glasgow, Glasgow, G12 8QQ, United Kingdom.

^fDepartment of Chemistry, University College London, London, WC1H 0AJ, United Kingdom.

Abstract

The formation of mixed-metal cobalt oxides, representing potential metal-support compounds for cobalt-based catalysts, has been observed at high conversion levels in the Fischer-Tropsch synthesis over metal oxide-supported cobalt catalysts. An often observed increase in the carbon dioxide selectivity at Fischer-Tropsch conversion levels above 80% has been suggested to be associated to the formation of water-gas shift active oxidic cobalt species. Mixed-metal cobalt oxides, namely cobalt aluminate and cobalt

¹ Present address: Institute of Chemical Reaction Engineering, University of Erlangen-Nuremberg, 91058 Erlangen, Germany

titanate, were therefore synthesised and tested for potential catalytic activity in the water-gas shift reaction. We present a preparation route for amorphous mixed-metal oxides via thermal treatment of metal precursors in benzyl alcohol. Calcination of the as prepared nanoparticles results in highly crystalline phases. The nano-particulate mixed-metal cobalt oxides were thoroughly analysed by means of X-ray diffraction, Raman spectroscopy, temperature-programmed reduction, X-ray absorption near edge structure spectroscopy, extended X-ray absorption fine structure, and high-resolution scanning transmission electron microscopy. This complementary characterisation of the synthesised materials allows for a distinct identification of the phases and their properties. The cobalt aluminate prepared has a cobalt-rich composition ($\text{Co}_{1+x}\text{Al}_{2-x}\text{O}_4$) with a homogeneous atomic distribution throughout the nano-particulate structures, while the perovskite-type cobalt titanate (CoTiO_3) features cobalt-lean smaller particles associated with larger ones with an increased concentration of cobalt. The cobalt aluminate prepared showed no water-gas shift activity in the medium-shift temperature range, while the cobalt titanate sample catalysed the conversion of water and carbon monoxide to hydrogen and carbon dioxide after an extended activation period. However, this perovskite underwent vast restructuring forming metallic cobalt, a known catalyst for the water-gas shift reaction at temperatures exceeding typical conditions for the cobalt-based Fischer-Tropsch synthesis, and anatase- TiO_2 . The partial reduction of the mixed-metal oxide and segregation was identified by means of post-run characterisation using X-ray diffraction, Raman spectroscopy, and transmission electron microscopy energy-dispersive spectrometry.

1. Introduction

The Co-based Fischer-Tropsch synthesis (FTS) converts synthesis gas to long-chained hydrocarbons and water (Equation 1).^{1,2} In contrast to the representative reaction equation forming a CH_2 chain segment, the actual consumption rate of H_2/CO under industrially relevant low temperature Fischer-Tropsch (FT) conditions is ~ 2.1 .^{1,3} However, increased conversion levels outside commercial relevance ($>80\%$ CO conversion) are reported to result in a pronounced consumption of CO when compared to H_2 , *i.e.* the H_2/CO ratio increases.⁴ This observation is typically accompanied by an increased selectivity towards CO_2 suggesting the conversion of CO and the FT product H_2O to CO_2 *via* the water-gas shift (WGS) reaction (Equation 2).⁴⁻⁹ However, the WGS activity of metallic Co^0 is negligible in the low temperature FTS (210-240 °C).^{3,10} Hence, a potential WGS activity has been associated to oxidic cobalt species,^{4,5,7-9} which may form upon phase transformation of the metallic FT active Co^0 phase during intrinsic exposure to H_2O -rich high conversion environment.¹¹⁻¹⁵ In particular, the formation of CoO and metal-support compounds has been suggested to drive this change in catalytic WGS activity.^{4,5,7-9} In general, the formation of CoO ^{4,12,13,16-19} and mixed-metal cobalt

oxides¹¹⁻¹⁵ is expected at high FT conversion levels due to the increased concentration of H₂O, which may induce oxidation and/or a solid state reaction between the active metallic Co⁰ phase and widely applied metal oxide carriers (Al₂O₃, SiO₂, TiO₂) resulting in metal-support compounds (MSCs). The formation of MSCs, such as cobalt aluminate or titanate, probably proceeds *via* a partially oxidised cobalt species.^{11,13,17} Recently, the formation of CoAl₂O₄ and CoTiO₃ has been directly monitored by means of *in situ* X-ray absorption near edge structure (XANES) during FTS over a Re-Co/Al₂O₃ and a Co/TiO₃ catalyst, respectively.^{13,15}



In the present study, we report the preparation and detailed characterisation of nanoparticulate mixed-metal cobalt oxides, namely cobalt aluminate and cobalt titanate, which were tested for catalytic activity in the WGS reaction. Our work investigates the potential link of the presence of these phases to the reported increased CO₂ selectivities at high conversion levels in the Co-based FTS.⁴⁻⁹ The mixed-metal cobalt oxides were synthesised based on a combined and modified approach according to reported sol-gel routes in benzyl alcohol.²⁰⁻²² In contrast to the published procedure for the preparation of cobalt aluminate (CoAl₂O₄) nanoparticles,²⁰ the synthesis of cobalt titanate (CoTiO₃) *via* the benzyl alcohol route has not been reported previously. Benzyl alcohol is a versatile solvent for surfactant-free non-aqueous sol-gel routes as it reacts with a broad range of metal precursors at moderate temperatures enabling a facile synthesis of numerous metal oxides *via* heat treatment in an open or closed reaction vessel.²³

2. Materials and methods

2.1 Synthesis of mixed-metal cobalt oxides

The preparation route of the mixed-metal cobalt oxides is based on a combined approach according to published sol-gel syntheses in benzyl alcohol for the synthesis of cobalt aluminate nanoparticles an autoclave²⁰ and a gram-scale route for the controlled synthesis of well-defined cobalt oxide nanoparticles.²² In short, 14 mmol (2859 mg) of aluminium(III) isopropoxide (AlC₉H₂₁O₃, Sigma-Aldrich, ≥98%) or 7 mmol (2382 mg) of titanium(IV) butoxide (TiC₁₆H₃₆O₄, Sigma-Aldrich, ≥97%) were dissolved in 140 mL benzyl alcohol (C₇H₈O, Sigma-Aldrich, ≥99%) together with 7 mmol (1744 mg) of cobalt(II) acetate tetrahydrate (Co(CH₃CO₂)₂·4H₂O, Sigma-Aldrich, Figure S1) under magnetic stirring at 600 rpm for the synthesis of cobalt(II) aluminate (CoAl₂O₄) or cobalt(II) titanate (CoTiO₃), respectively. After complete dissolution, the 500 mL rotary round bottom flask (500 mL) was transferred to a pre-heated oil bath (180 °C) of a rotary evaporator set-up, rotated at 180 rpm and heat-treated for 12 h at an absolute pressure of 900 mbar. Air was bubbled through the synthesis solution throughout the heat

treatment ensuring adequate mixing.²² After cool-down to room temperature, the volume was tripled with diethyl ether ((C₂H₅)₂O, Kimix (South Africa), ≥99%) and the mixture was centrifuged for 1 hour at 7000 rpm. The centrifugate containing the nanoparticles was re-dispersed in ethanol (CH₃OH, Kimix, ≥99.9%) and washed at least three times with acetone (CH₃COCH₃, Kimix (South Africa), ≥99.3%) until a clear supernatant was obtained. A fraction of the collected nanoparticles was calcined in a ceramic bowl in an oven (Memmert) at 600 °C for 12 h (5 °C min⁻¹), while the remaining part was applied in catalytic testing without further treatment.

A bulk-sized CoAl₂O₄ structure was synthesised *via* co-precipitation for reference purposes. At first, cobalt(II) acetate tetrahydrate (2820 mg) and aluminium(III) isopropoxide (4620 mg) were dissolved in 400 mL 1-butanol (C₄H₉OH, Merck, ≥99.0%). A 0.1 M sodium hydroxide (NaOH, Kimix) solution was added dropwise under magnetic stirring at 50 °C until reaching a pH of 8 in order to initiate precipitation. The precipitate was subsequently washed with H₂O, filtered, and dried at 120 °C. The sample was calcined in an oven (Nabertherm) at 1000 °C (7.5 °C min⁻¹) for 3 h yielding a mixture of cobalt aluminate, sodium aluminate and alumina due to the provided excess of the aluminium precursor.

2.2 Synthesis of single phase cobalt oxides

Single phase CoO and Co₃O₄ nanoparticles (Figure S2-S3) were prepared as reference compounds according to a previously described gram-scale route for the controlled synthesis of well-defined nanoparticles.²² For this, 12.85 mmol (3200 mg) of cobalt(II) acetate tetrahydrate was dissolved in 140 mL of benzyl alcohol in a 500 mL rotary round bottom flask under magnetic stirring at 600 rpm for both oxides. After complete dissolution, 140 mL of ammonia solution (NH₄OH_(aq), Kimix, min 25%) were added drop-wise or 8510 mg of ammonium acetate (NH₄CH₃CO₂, Merck, ≥97.0%) was dissolved in the solution for the synthesis of Co₃O₄ or CoO nanoparticles, respectively. Subsequently, the flask was transferred to a pre-heated oil bath (165 °C) of a rotary evaporator set-up, rotated at 180 rpm and heat-treated for 3 h at an absolute pressure of 900 mbar. Air was bubbled through the solution throughout the heat treatment ensuring adequate mixing.²² After cool-down to room temperature, the nanoparticles were collected and washed in the same manner as the mixed-metal cobalt oxides.

2.3 Characterisation

X-ray diffraction (XRD) was conducted at 35 kV and 40 mA in a D8 Advance X-ray diffractometer (Bruker AXS), equipped with a cobalt source ($\lambda_{\text{Co}} = 1.78897 \text{ \AA}$; slit width = 1.0 mm) and a LYNXEYE XE position sensitive detector (Bruker AXS) from 20-120° at a step size of 0.025° with an exposure time of 1 s per step. Obtained XRD patterns were compared to reference patterns of the Powder Diffraction File of the International

Centre for Diffraction Data (ICDD; PDF-2 Release 2008;²⁴ CoAl₂O₄: 00-003-0896, Co₃O₄: 00-043-1003, CoTiO₃: 00-015-0866; a-TiO₂: 01-086-1157; hcp-Co: 01-071-4239). Volume-mean crystallite sizes and weight fractions of the particular phases with associated errors were determined by Rietveld refinement of the XRD patterns (TOPAS 5, Bruker AXS).²⁵ The instrumental line broadening was modelled *via* fitting an obtained pattern of corundum with additional convolutions exclusively. Additional diffraction line broadening analysis *via* the Scherrer equation²⁶ (Co₃O₄ and CoAl₂O₄: 311 diffraction; CoTiO₃: 211 diffraction) with correction for the instrumental line broadening and a shape factor of 0.9 was applied as a second method to estimate the crystallite size.²⁷

Analysis of samples *via* Raman spectroscopy was conducted in an inVia Raman microscope (Renishaw) with a wavelength of the laser of 532 nm. The Raman laser was fitted with a compact fibre optics probe (Renishaw). Five repetitions were taken at 40 mW laser power and an exposure time of 30 s.

For elemental analysis by means of inductively coupled plasma optical emission spectrometry (ICP-OES), the samples prepared were treated with 5 mL of 40 wt.% HF and the solution was boiled to dryness. Thereafter, 6 mL of 40 wt.% HF were added and the solution was boiled until the volume was reduced to 1 mL. Subsequently, 6 mL of 65 wt.% HNO₃ was added and the solution was, once again, boiled until the volume was reduced to 1 mL. After several addition-reduction cycles, the solution was transferred into a Teflon digestion vessel and mixed with 10 mL aqua regia. The solutions were heated at a heating rate of 3 °C min⁻¹ to 180 °C for 30 min during microwave digestion (1600 W) and analysed in a Varian ICP-OES 730.

Temperature programmed reduction (TPR) was conducted using an AutoChem II 2920 (Micromeritics). Volatile organic compounds and water were removed at 200 °C (10 °C min⁻¹) in Ar for 2 h prior to analysis. H₂ consumption was acquired in a 5% H₂/Ar atmosphere from 50-950 °C with a heating ramp of 10 °C min⁻¹ and a holding time of 0.5 h at 950 °C of 0.5 h. H₂ consumption peaks were fitted in MATLAB²⁸ utilising the peakfit.m script²⁹ of the file exchange database.

X-ray absorption near edge structure (XANES) spectra at the Co K-edge were obtained at beamline B18 (beamtime number sp15151) of the Diamond Light Source in Harwell (United Kingdom).³⁰ The samples were analysed in transmission mode with three repetitions. All spectra were acquired with a Co foil placed before the reference detector. The raw data was processed in Athena of the open-source software package Demeter,³¹ which is based on the IFEFFIT³² library. Fourier transforms of the k² weighted extended X-ray absorption fine structure (EXAFS) spectra were obtained applying phase correction and using a 9 Å⁻¹ Hanning-type window in Athena.

The prepared mixed-metal cobalt oxides were analysed by means of high-resolution scanning transmission electron microscopy (HRSTEM). The samples were dispersed in ethanol *via* ultrasonication for 30 min prior to deposition onto Quantifoil sample grids

for analysis. HRSTEM images were acquired at atomic resolution using double spherical aberration corrected JEM-ARM200F microscope (JEOL). The samples were studied with bright field and dark field imaging. A GIF electron spectrometer with dual electron energy loss spectrometry (EELS) imaging capabilities and an XMax 100 TLE high collection angle, ultra-sensitive detector (Oxford Instruments) was applied for analysis by means of energy-dispersive spectrometry (EDS).

Transmission electron microscopy energy-dispersive spectrometry (TEM-EDS) was conducted using a Tecnai F20 microscope (Philips) equipped with a field emission gun using a grid tilt of 45° and operated at 200 kV (Gatan). Imaging was done with a US4000 4kX4k CCD camera (Gatan). The TEM is equipped with a XFlash 6TI60 (Bruker) detector for EDS. Spectra were analysed using the QUANTAX ESPRIT 2.1 software (Bruker). The samples were analysed after catalytic measurements and dispersed in acetone *via* ultrasonication for 1 min prior to deposition onto carbon-coated copper grids.

2.4 Catalytic testing

Catalyst performance testing of the synthesised mixed-metal cobalt oxides was conducted in the high throughput Flowrence (Avantium) reactor setup according to a previously described procedure using quartz reactor tubes.³³ The catalytic WGS activity of 140 mg mixed-metal cobalt oxide was evaluated at atmospheric pressure and two reaction temperatures in the medium shift range, *viz.* 275 and 325 °C. A nominal high-temperature shift gas feed consisting of 75% H₂, 10% CO, 10% CO₂, and 5% Ar on a dry basis was applied with a steam to dry gas ratio of 1:2 – such that the ultimate feed was 50% H₂, 6.67% CO, 6.67% CO₂, 3.33% Ar and 33.33% H₂O. The space velocity was 15000 mL_{STP} g_{cat}⁻¹ h⁻¹ for the first 110 h time on stream (TOS) and was subsequently reduced to 7500 mL_{STP} g_{cat}⁻¹ h⁻¹ to allow for increased conversion levels. Analysis of the effluent was performed using a CP-490 micro-GC (Agilent) equipped with a COX column in order to determine the CO conversion.

3. Results and discussion

3.1 Synthesis and characterisation

The collected solid nanoparticles from the synthesis targeting CoAl₂O₄ have a dark-blue colour. The colour of divalent Co stereochemically depends on the coordination site and number and hence provides information on the environment of the particular cobalt cation. Tetrahedral Co²⁺ is blue for various Co(II) complexes such as [CoCl₄]²⁻, as well as for the divalent Co in CoAl₂O₄.³⁴ The dark-blue colour of the powder obtained may indicate the additional presence of Co₃O₄, trivalent Co³⁺ in an inverse CoAl₂O₄ spinel, or a partial substitution of trivalent Al³⁺ with Co³⁺ resulting in a Co-rich

aluminate. In all cases, the occupancy of the octahedral void by Co^{3+} is expected to result in a black colour as observed for single phase Co_3O_4 . Conducting the same synthesis procedure with titanium butoxide instead of aluminium isopropoxide as precursor for the second metal resulted in a green powder indicating the successful formation of perovskite-type cobalt titanate³⁵ (CoTiO_3 , respectively TiCoO_3 according to the ABO_3 notation for perovskites with A being the cation with the larger radius). Elemental analysis by means of ICP-OES of both samples prepared results in 26.0 and 24.6 wt.% Co for the cobalt aluminate (Al: 22.6 wt.%) and the cobalt titanate (Ti: 19.4 wt.%), respectively. The lower fraction of Co, when compared to the theoretical values (CoAl_2O_4 : 33 wt.%; CoTiO_3 : 38 wt.%), is most likely due to organic residuals originated in the synthesis in benzyl alcohol,²² which is also indicated by the reduced fractions of the particular second metal resulting in molar ratios of Al:Co and Ti:Co of 1.90 and 0.97 (CoAl_2O_4 : Al:Co = 2; CoTiO_3 : Ti:Co = 1), respectively. Further, the authors note that the challenging digestion of the samples prepared results in rather large uncertainties of approximately 2 wt.%.

Analysis of the as prepared powders by means of XRD reveals the amorphous character of both samples, which could be transformed into crystalline structures through calcination at 600 °C for 12 h in stagnant air (Figure 1a). The formation of amorphous phases indicates the necessity of temperatures above the boiling point of the solvent for a one-step preparation of crystalline materials. For example, Karmaoui *et al.* obtained crystalline material when synthesising cobalt aluminate *via* the benzyl alcohol route in autoclaves allowing for temperatures above the boiling point of benzyl alcohol and vapour pressures exceeding 1 bar.²⁰ A distinct differentiation of the diffraction pattern of CoAl_2O_4 with that of Co_3O_4 is challenging as both form a spinel. However, Co_3O_4 has a marginally shorter edge length of the cubic unit-cell (8.08370 vs. 8.10658 Å).^{36,37} Indeed, comparison of the XRD pattern obtained with the pattern for the synthesised Co_3O_4 nanoparticles indicates a slight shift of the diffractions to lower angles (Figure 1b). Further, modelling the pattern obtained for the Co_3O_4 reference sample and the calcined cobalt aluminate sample with a spinel structures *via* Rietveld refinement results in a shorter edge length for the Co_3O_4 sample than for the crystalline cobalt aluminate (8.081 vs. 8.097 Å). Another indication of the formation of cobalt aluminate is the volume-mean crystallite size of 4.4 ± 0.1 nm (3.5 nm according to Scherrer equation), which is small given the prolonged calcination at 600 °C. The crystallite size can be expected to be significantly larger for Co_3O_4 due its lower thermal stability resulting in pronounced sintering. Lastly, the absence of the (III) diffraction peak at 22° indicates the successful synthesis of cobalt aluminate as well. However, reported patterns in literature are inconsistent as this diffraction peak is observed in several publications,³⁷⁻³⁹ but absent in others.^{40,41}

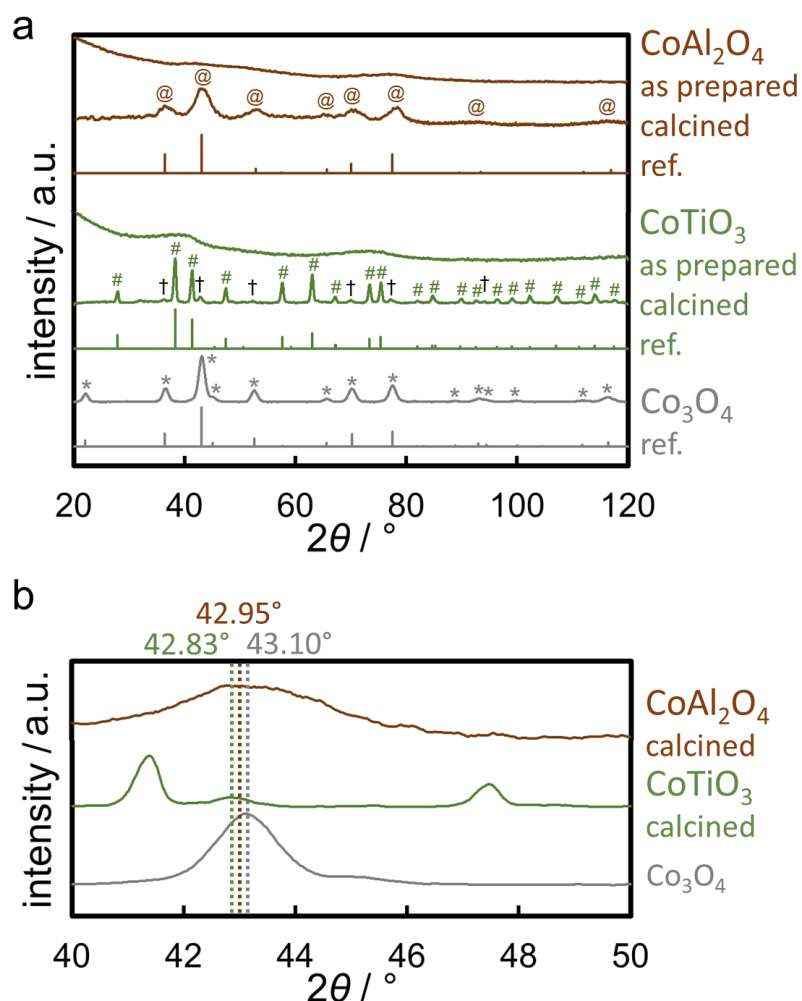


Figure 1 X-ray diffraction patterns of the nanoparticles synthesised via the benzyl alcohol route targeting CoAl_2O_4 and CoTiO_3 (a) before and after calcination at 600°C for 12 h with identified diffraction peaks of CoAl_2O_4 (@), CoTiO_3 (#), and a spinel structure (†) with a pattern of nano-sized Co_3O_4 (*) for comparison, as well as reference patterns for the particular compounds. (b) Enlarged 311 diffraction of the calcined mixed-metal cobalt oxides and Co_3O_4 with the angles of maximum intensity.

The XRD pattern of the collected and calcined solid sample from the synthesis targeting CoTiO_3 mostly resembles the reference pattern of CoTiO_3 (Figure 1a). The presence of a small fraction of a spinel phase is suggested by the additional diffraction peaks (e.g. 37.5° , 43.0° , 70.2° , and 77.5°) and Rietveld refinement with CoTiO_3 and Co_3O_4 (representing any spinel) results in a potential impurity of $\sim 11 \pm 0.8$ wt.%. We note that the volume-mean crystallite size of this phase is smaller than for the CoTiO_3 (Rietveld refinement: 13.4 vs. 22.6 nm; Scherrer equation: 12.9 vs. 16.4 nm), which suggests the presence of a spinel other than the thermally less stable Co_3O_4 . Hence, the impurities may represent the spinel Co_2TiO_4 , i.e. Ti^{4+} cations may be incorporated in the spinel structure of Co_3O_4 , which is supported by the larger shift of the 311 diffraction peak to

lower angles due to an extended edge length of the cubic unit-cell for Co_2TiO_4 when compared to Co_3O_4 (8.42000 vs. 8.08370 Å).^{36,42}

Analysis by Raman spectroscopy was conducted in order to verify the phases identified after calcination from XRD analysis. In addition, Raman spectroscopy allows the identification of amorphous species. The as prepared powder and the calcined sample of the sol-gel synthesis targeting CoAl_2O_4 display similar Raman spectra (Figure S4). In fact, the spectra only differ in the width of the particular peaks, which may be explained by an increase of the crystallite size after calcination. Size-dependent peak shapes in Raman spectroscopy have been previously reported for Co_3O_4 and Mn_3O_4 .^{12,43} Hence, calcination of the as prepared amorphous phase induces a re-arrangement of the initially disordered ions resulting in the same phase with a high crystallinity and increased particle size. The Raman spectra for the cobalt aluminate sample feature several characteristics of the spectrum of Co_3O_4 nanoparticles (Figure 2), but the peaks at 197 and 611 cm^{-1} are more pronounced and the 685 cm^{-1} peak displays a distinct shoulder to higher Raman shifts. The Raman spectrum obtained resembles spectra of CoAl_2O_4 from the literature.⁴⁴ However, comparison with a study on the preparation and characterisation of cobalt aluminates with varying Al:Co ratios ($\text{Co}_{1+x}\text{Al}_{2-x}\text{O}_4$) indicates a Co-rich composition of our prepared aluminate with x being in the range of 0.5-0.8,³⁸ which would be in line with the dark-blue colour that was observed. The Raman spectrum for an ideal 2:1 ratio of Al:Co differs strongly from spectra of Co-rich samples featuring peaks at 202, 408, and 511 cm^{-1} , which was confirmed in the present study analysing a precipitated bulk CoAl_2O_4 sample (Figure S4) containing impurities of Al_2O_3 and sodium aluminate in order to avoid the formation of a Co-rich aluminate.

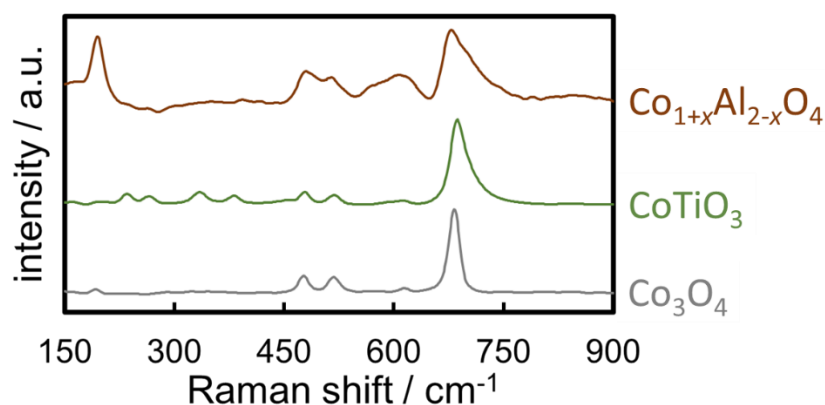


Figure 2 Raman spectra of the nanoparticles synthesised via the benzyl alcohol route targeting CoAl_2O_4 and CoTiO_3 after calcination at 600 °C for 12 h with a spectrum of nano-sized Co_3O_4 for comparison.

In contrast to the Raman spectrum of the calcined cobalt aluminate sample, the synthesised and calcined cobalt titanate matches with published spectra for CoTiO_3 ^{35,45-47} with major peaks at 240, 270, 339, 388, 617, and 687 cm^{-1} (Figure 2). However, once again the Raman spectra in the literature are contradictory. In particular the peaks at

481 and 521 cm^{-1} are inconsistently identified for CoTiO_3 samples in previously published work.^{35,45}

Mixed-metal cobalt oxides not only exhibit an increased thermal stability when compared to cobalt oxide, but are also more difficult to reduce in H_2 -containing atmospheres.⁴⁸ TPR is a commonly applied characterisation technique for such hard-to-reduce species and has been applied for the calcined mixed-metal cobalt oxide samples. High temperature peaks in the profile of the H_2 consumption are identified for both samples during TPR (Figure 3). The profiles differ strongly from a Co_3O_4 sample exhibiting the high stability against reduction by H_2 . TPR analysis of the cobalt titanate sample results in a narrow H_2 consumption peak in the same temperature range (450-780 $^\circ\text{C}$) as reported for perovskite-type CoTiO_3 (Figure 3).⁴⁹ The overall consumption of H_2 , obtained *via* deconvolution of said peak with two Gaussians, approximates the expected amount of H_2 required for reduction of CoTiO_3 to Co , TiO_2 , and H_2O (Table S1). Further, the peak area of the deconvoluted low temperature reduction peak at 587 $^\circ\text{C}$ contributes about 31% to the overall consumption of H_2 (Table S2). In contrast, the profile of the calcined $\text{Co}_{1+x}\text{Al}_{2-x}\text{O}_4$ sample indicates reduction within a wide temperature range, particularly when compared to the bulk CoAl_2O_4 sample ($\Delta T = 350$ $^\circ\text{C}$ vs. 120 $^\circ\text{C}$; Figure S5). This reduction behaviour may suggest the reduction of an inhomogeneous phase, *i.e.* the particular compositions in the $\text{Co}_{1+x}\text{Al}_{2-x}\text{O}_4$ sample may result in reduction over a broad temperature range. Peak deconvolution with four Gaussians suggests that 51% of the H_2 consumption are due to the main peak at 756 $^\circ\text{C}$ (Table S3). Contrary, most of the H_2 consumption is observed at temperatures exceeding 800 $^\circ\text{C}$ in the reference CoAl_2O_4 sample (Figure S5; Table S4). Once again, this observation supports the suggested Co-rich composition of our prepared aluminate allowing for reduction at reduced temperatures. Further, the overall consumption of H_2 during TPR of $\text{Co}_{1+x}\text{Al}_{2-x}\text{O}_4$ exceeds the expected consumption for abstraction of one oxygen atom from aluminate forming Co , Al_2O_3 , and H_2O by 27% (Table S1), *i.e.* the Co-rich nature allows for an increased reducibility of the sample when compared to cobalt aluminate with an atomic ratio of Co:Al of 1:2.

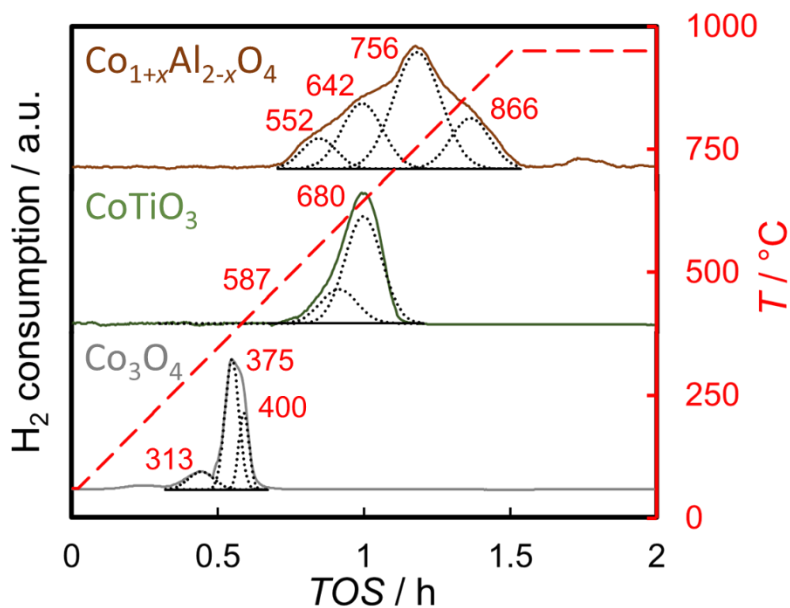


Figure 3 Temperature programmed reduction profiles with deconvoluted peaks of $\text{Co}_{1+x}\text{Al}_{2-x}\text{O}_4$ and CoTiO_3 nanoparticles synthesised via the benzyl alcohol route after calcination at 600 °C for 12 h, as well as of nano-sized Co_3O_4 for comparison.

The mixed-metal oxides $\text{Co}_{1+x}\text{Al}_{2-x}\text{O}_4$ and CoTiO_3 were further characterised by XANES at the Co K-edge. The spectra obtained strongly resemble published spectra of cobalt aluminate^{17,50,51} and cobalt titanate¹⁵ confirming the successful preparation of the particular mixed-metal cobalt oxides (Figure 4). The white line characteristics for single phase and mixed-metal cobalt oxides dominate the near-edge structure, while unique features at energies above the white line allow for a clear distinction between the cobaltous species. In contrast to its oxidic counterparts, metallic Co has a distinct pre-edge feature (Figure 4, Table S5). A linear dependency of the edge shift to higher energies with increased valency of a metal has been reported.⁵² This relationship is also observed for the synthesised single-phase cobalt oxide references (Figure 5, Table S5) as reported in literature.^{53,54} The edge shift of the CoTiO_3 sample relative to the K-edge of metallic Co^0 is smaller than expected for the case of a linear dependency. The synthesised cobalt aluminate sample shows an even less pronounced edge shift (1.0 eV), while the valency can be expected to be larger than two due to the proposed Co-rich composition. However, the additionally analysed bulk sample of CoAl_2O_4 with a 2:1 ratio of Al:Co has a small edge shift of 1.1 eV as well (Figure S6). In general, all features in the XANES spectrum of the bulk CoAl_2O_4 phase are more pronounced than in the synthesised $\text{Co}_{1+x}\text{Al}_{2-x}\text{O}_4$, *i.e.* the shape of the spectrum is well-defined, which is most probably related to the large difference in the crystallite size.⁵⁵ However, the normalised pre-edge and white line intensities are comparable, *i.e.* both samples seemingly have a similar average oxidation state of Co (Figure 4, Table S5).

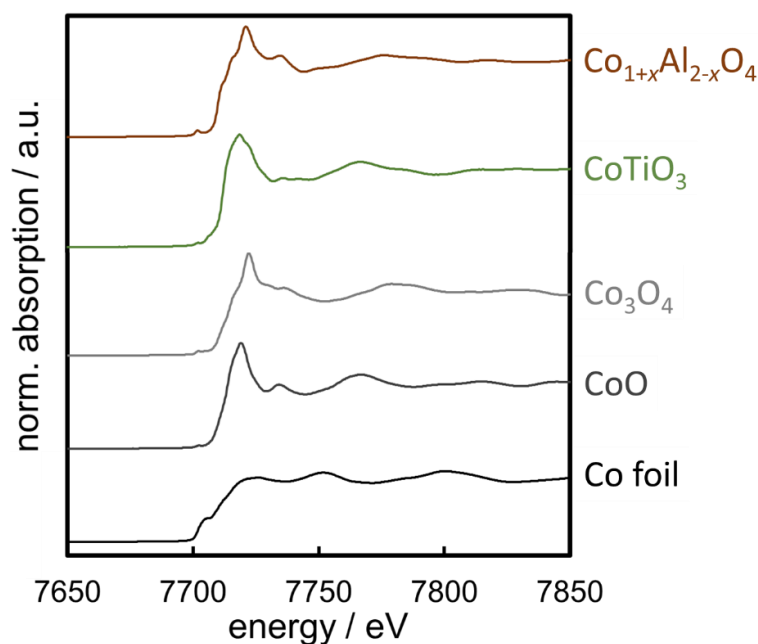


Figure 4 Normalised X-ray absorption fine structure spectra of $\text{Co}_{1+x}\text{Al}_{2-x}\text{O}_4$ and CoTiO_3 nanoparticles synthesised *via* the benzyl alcohol route after calcination at 600°C for 12 h and a reference spectrum of cobalt foil.

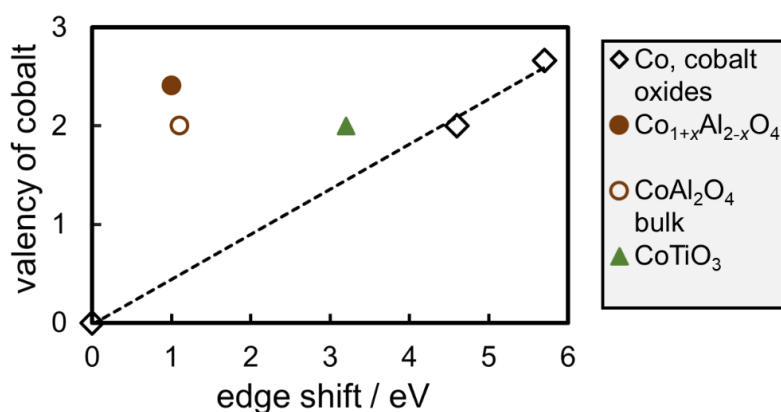


Figure 5 Dependency of the energy shift of the cobalt K-edge in X-ray adsorption near-edge structure spectroscopy and the oxidation state of cobalt for cobalt oxides (linear dependency, dashed) and mixed-metal cobalt oxides relative to the edge of cobalt foil.

Fourier transformation of the spectra acquired provides the EXAFS spectra of the samples prepared (Figure 6). The resulting radial distances for the Co-O shell are similar for the cobalt aluminate sample prepared, the bulk aluminate, and nano-sized Co_3O_4 (1.79, 1.81, and 1.78 Å, respectively), which is originated in the spinel structure in these samples. The less pronounced structural peaks, once again, suggest a smaller average particle size of the aluminate prepared when compared to the precipitated sample.⁵⁵ The radial distance for Co-O is increased to 1.91 Å for the perovskite-type CoTiO_3 , while said radial distance in the reference samples is in line with literature values (Figure S7; Table S6).^{50,53,56,57}

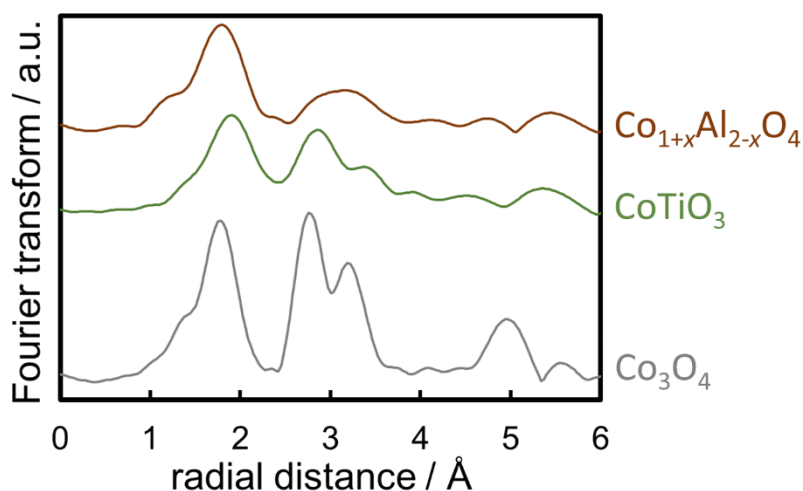


Figure 6 Radial distances as obtained after phase corrected Fourier transform of extended X-ray absorption fine structure spectra of $\text{Co}_{1+x}\text{Al}_{2-x}\text{O}_4$ and CoTiO_3 nanoparticles synthesised *via* the benzyl alcohol route after calcination at $600\text{ }^\circ\text{C}$ for 12 h, as well as Co_3O_4 nanoparticles.

Analysis of the synthesised $\text{Co}_{1+x}\text{Al}_{2-x}\text{O}_4$ sample by means of HRSTEM exhibits the high crystallinity obtained during calcination at $600\text{ }^\circ\text{C}$ (Figure 7). Furthermore, the sample consists of intergrown domains as one particle features various crystalline orientations. The initially smaller amorphous nanoparticles probably formed a crystalline structure prior to the thermally induced sintering process forming enlarged particles. Hence, the volume-mean crystallite size of 4.4 nm , as obtained by means of XRD, only represents the average size of these crystalline domains and the particle size is significantly larger (Figure 7a). Size analysis of these domains results in a number-mean crystallite size of 5.3 nm , which supports this conclusion. Elemental mapping *via* electron energy loss spectroscopy (EELS) reveals a uniform distribution of the metal atoms (Figure 8; Figure S8). Some Co-rich areas can be identified, which supports the suggested synthesis of a Co-rich aluminate resulting in localised differences in the atomic composition. However, the distribution of Co and Al is fairly homogeneous.

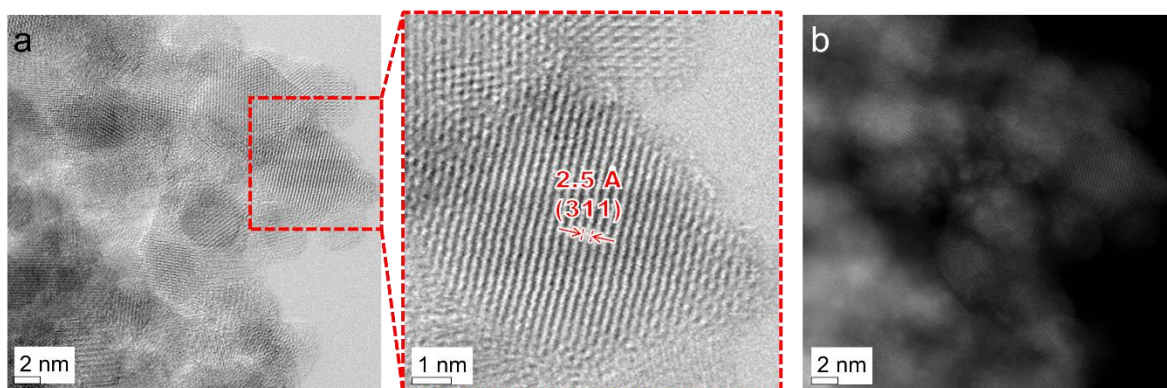


Figure 7 High-resolution (a) bright-field scanning transmission electron micrograph with a magnified inset exhibiting the d-spacing of the major (311) lattice plane of CoAl_2O_4 and (b) high angular annual dark-field micrograph of $\text{Co}_{1+x}\text{Al}_{2-x}\text{O}_4$ nanoparticles synthesised *via* the benzyl alcohol route after calcination at 600°C for 12 h.

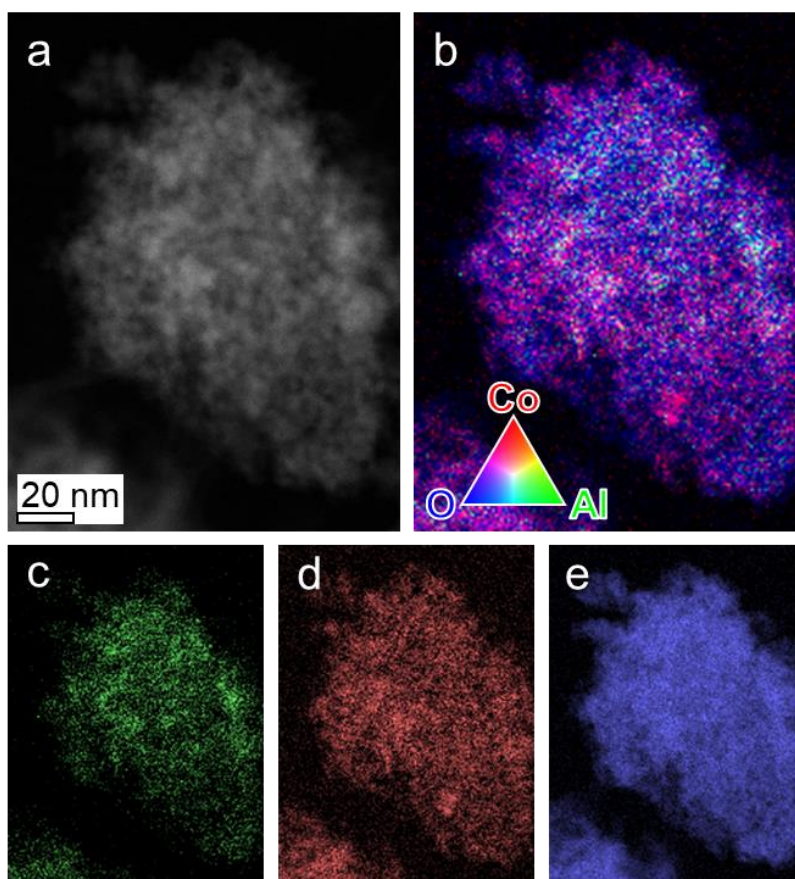


Figure 8 (a) High-resolution high angular annual dark-field scanning transmission electron micrograph of $\text{Co}_{1+x}\text{Al}_{2-x}\text{O}_4$ nanoparticles synthesised *via* the benzyl alcohol route after calcination at 600°C for 12 h with (b) an elemental mapping as obtained *via* electron energy loss spectroscopy and the particular contributions of (c) aluminium, (d) cobalt, and (e) oxygen.

Similar results were obtained when analysing the synthesised and calcined CoTiO_3 sample by means of HRSTEM (Figure 9). Once again, intergrown crystallites form enlarged particles. In addition, a smaller and a larger particle size range were identified (Figure 10; Figure S9). EELS analysis suggests a lower concentration of Co atoms in smaller particles. However, elemental mapping confirms the presence of Co in all particles (Figure 10; Figure S9). The formation of various compositions is in line with observed TPR peaks over a wide temperature range and more pronounced than in the $\text{Co}_{1+x}\text{Al}_{2-x}\text{O}_4$ sample (Figure 8).

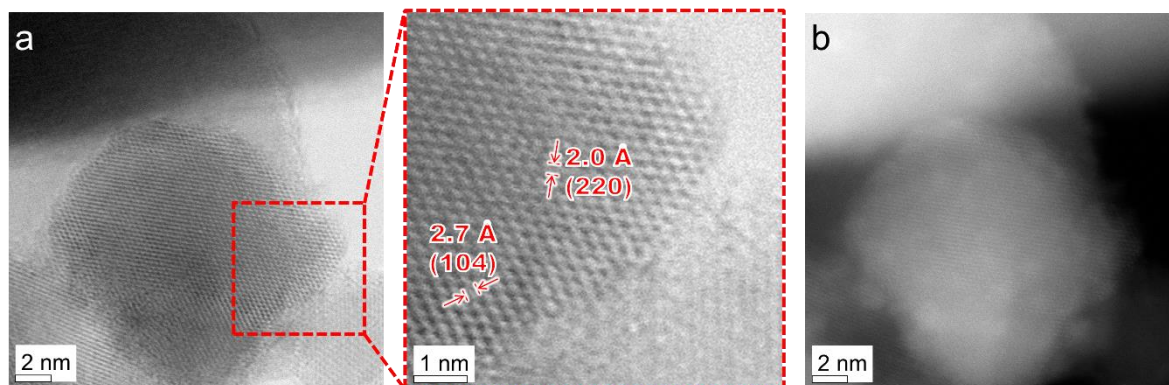


Figure 9 High-resolution (a) bright-field scanning transmission electron micrograph with a magnified inset exhibiting d-spacings of major lattice planes of CoTiO_3 and (b) high angular annular dark-field micrograph of CoTiO_3 nanoparticles synthesised via the benzyl alcohol route after calcination at 600 °C for 12 h.

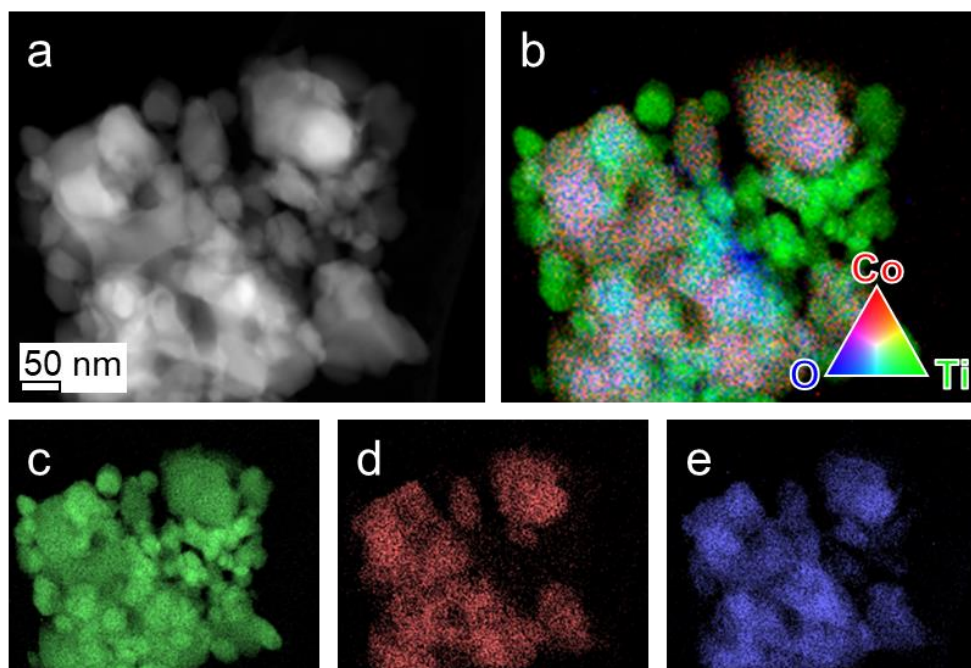


Figure 10 (a) High-resolution high angular annular dark-field scanning transmission electron micrograph of CoTiO_3 nanoparticles synthesised via the benzyl alcohol route after calcination at $600\text{ }^\circ\text{C}$ for 12 h with (b) an elemental mapping as obtained via electron energy loss spectroscopy and the particular contributions of (c) titanium, (d) cobalt, and (e) oxygen.

3.2 Water-gas shift activity testing

The as prepared and the calcined cobalt aluminate ($\text{Co}_{1+x}\text{Al}_{2-x}\text{O}_4$) samples were tested for WGS activity using typical high-temperature shift gas feed (15:10:2:2 H_2 : H_2O : CO_2 : CO). Both, the amorphous sample prior to thermal treatment and the crystalline sample after calcination showed just about zero conversion in the studied temperature range 275 - $325\text{ }^\circ\text{C}$ (Figure 11). This result strongly suggests no catalytic WGS activity of cobalt aluminate at given conditions. In contrast, testing the calcined CoTiO_3 sample resulted in 1-2% conversion of CO at $275\text{ }^\circ\text{C}$ and up to 8% conversion after increasing the temperature to $325\text{ }^\circ\text{C}$ (Figure 11). An activation period of 35-40 h upon increase of the temperature may indicate slow restructuring or phase transformation of the CoTiO_3 phase. The CO conversion was further increased by lowering the space velocity. No activation period is observed supporting the proposed thermally induced restructuring after increasing the reaction temperature to $325\text{ }^\circ\text{C}$. We note that conversions of 11-13% conversion are lower than the expected twofold increase of the CO conversion to $\sim 16\%$ as the space velocity was halved. Further, commercial $\text{Cu-ZnO}/\text{Al}_2\text{O}_3$ would easily yield equilibrium conversion at given conditions, *i.e.* the observed activity of the CoTiO_3 sample upon activation is low when compared to WGS catalysts, even though the latter would operate well above its designated optimal temperature range.⁵⁸

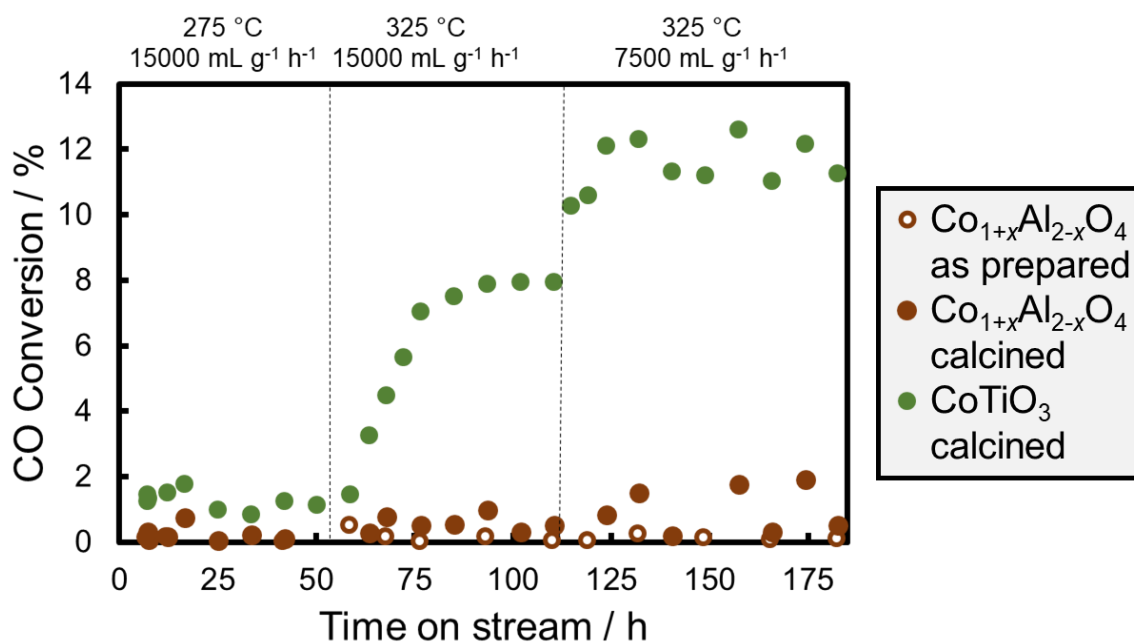


Figure 11 Conversion of CO during medium-temperature water-gas shift over mixed-metal cobalt oxides at 275 and 325 °C, as well as at 325 °C and halved gas hourly space velocity.

After catalytic testing, the spent samples were analysed by means of XRD (Figure 12). A crystalline phase is identified for the as prepared, amorphous cobalt aluminate after WGS activity measurements at 275 and 325 °C. Hence, this phase experienced significant restructuring resembling the sample after calcination in air at 600 °C. However, the volume-mean crystallite size is close to the detection limit and smaller when compared to the calcined sample (2.2 ± 0.1 vs. 4.4 ± 0.1 nm) and the expected crystalline fraction is less due to a pronounced contribution of the background. The second cobalt aluminate sample applied in catalytic testing after calcination in air did not undergo any significant phase transformation. Rietveld refinement resulted in a volume-mean crystallite size of 4.2 ± 0.1 nm similar to the size prior to catalytic testing (4.4 ± 0.1 nm). In line with these results from XRD analysis, the Raman spectrum of the spent cobalt aluminate resembles the one prior to catalytic measurements suggesting the absence of structural changes (Figure S10).

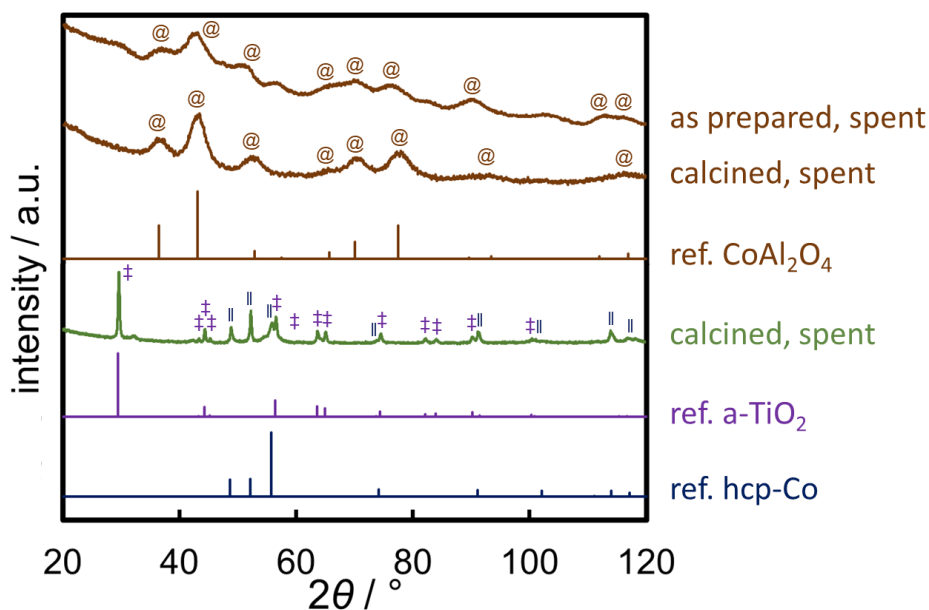


Figure 12 Post-run X-ray diffraction patterns of the nano-particulate cobalt aluminate with identified diffraction peaks of CoAl_2O_4 (@) and the cobalt titanate sample with identified diffraction peaks of anatase- TiO_2 (‡) and hcp-Co (||) after water-gas shift activity measurements with reference patterns of the particular compounds.

Analysis of the calcined CoTiO_3 sample after WGS activity testing by means of XRD exhibits vast phase transformations (Figure 12). A drastic shrinkage of the catalyst bed is a first indication for this previously proposed restructuring. Furthermore, no contribution of the initial perovskite-type mixed-metal cobalt oxide to the XRD pattern obtained during post-run analysis may be identified. Only anatase- TiO_2 (45.0 ± 0.6 nm) and hcp-Co (19.5 ± 0.3 nm) are identified, while Rietveld refinement results in a phase concentration of the latter metallic Co^0 phase of 29.6 ± 0.4 wt.%, which approximates the theoretical fraction of 38 wt.% as expected for full segregation of an ideal Co:Ti composition of 1:1. Further, an expected passivation layer of cobalt oxide, protecting metallic Co^0 from full oxidation after collection for post-run analysis due to its pyrophoric nature,⁵⁹ may be below the detection limit of XRD while reducing the phase fraction of metallic Co^0 .

Segregation of the CoTiO_3 sample during WGS activity measurements was confirmed using Raman spectroscopy and TEM-EDS. The Raman spectrum features the bands of a commercial anatase- TiO_2 (Sigma-Aldrich) sample and Co_3O_4 (Figure 13), which is the expected oxidic phase at the surface of cobaltous nanoparticles after exposure to air.⁵⁹ TEM-EDS revealed the inhomogeneous morphology of the spent sample consisting of particles with dimensions below 100 nm and a rather low density (Figure 14a), which resemble the structure of commercial anatase- TiO_2 (Figure S11). Smaller particles of less than 10 nm are seemingly associated to said larger particles and may represent the cobaltous phase. Indeed, a small contribution of Co was identified by means of EDS,

while the most abundant element in the area analysed *via* TEM is Ti (Figure 14b). Several large Co-rich structures may also be identified using TEM-EDS (Figure 14c,d). Hence, the bulk of the segregated Co^0 phase seemingly sintered forming large particles, while several smaller nanoparticles are supported on the anatase- TiO_2 structures. A relatively large metallic core may be expected in the particles resulting in sharp diffraction peaks in the XRD pattern of the particular spent CoTiO_3 sample (Figure 12).

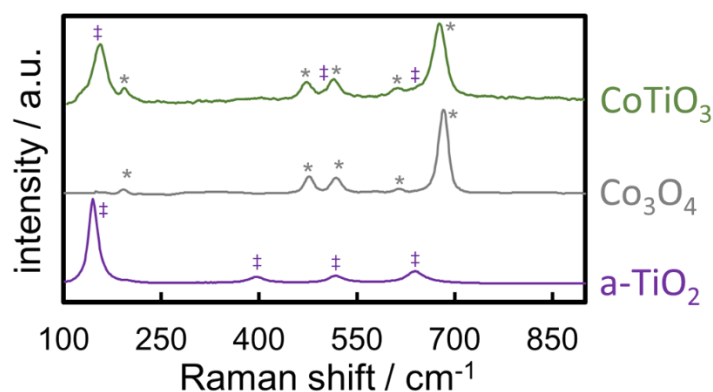


Figure 13 Post-run Raman spectra of the nano-particulate cobalt titanate with identified contributions of Co_3O_4 (*) and anatase- TiO_2 (‡) after water-gas shift activity measurements with spectra of nano-sized Co_3O_4 and anatase- TiO_2 for comparison.

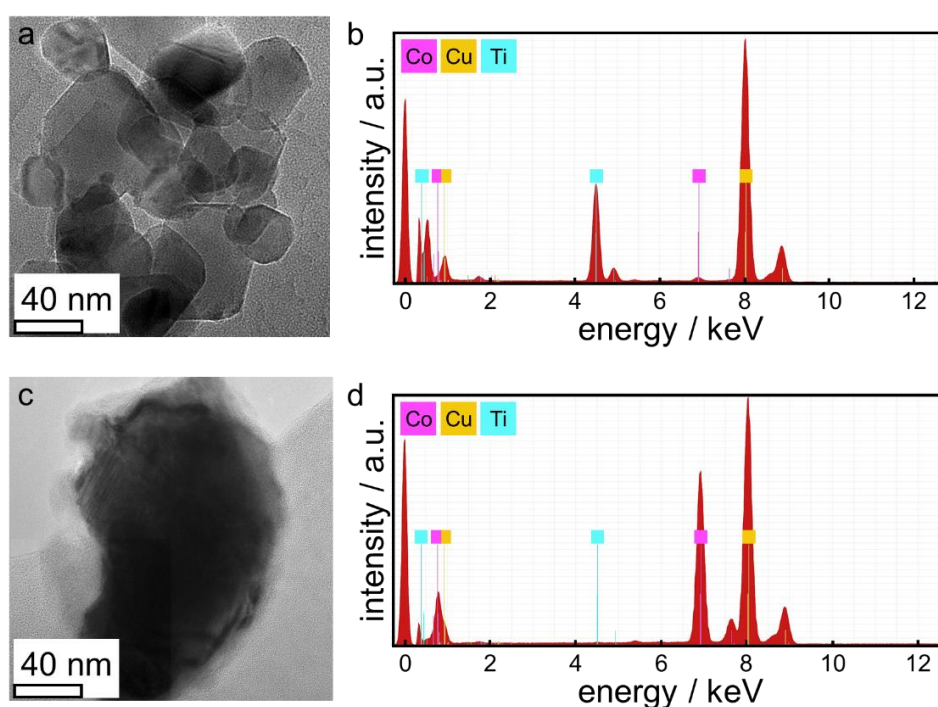


Figure 14 Post-run transmission electron micrographs of the nano-particulate cobalt titanate after water-gas shift activity measurements focussing on (a) a Ti-rich and (c) Co-rich microstructure with (b,d) the corresponding energy dispersive X-ray spectra. We note that the strong signal for Cu is originated in the use of carbon-coated copper grids.

The literature provides examples for a partial reduction of perovskites containing cobalt, which may result in segregation.^{60,61} Full segregation may be preceded by exsolution of Co^0 , an often described process for transition metals in the B site of perovskites.⁶²⁻⁶⁵ The extended time frame of the catalytic activation suggests a thermally induced, slow, and kinetically controlled phase transformation, *i.e.* a large fraction of the CoTiO_3 phase is converted after 35-40 h TOS at 325 °C. The resulting metallic Co^0 is a well-known catalyst for the WGS reaction at increased temperatures,^{3,10} which may explain the observed WGS activity of the perovskite sample during WGS testing (Figure II). Furthermore, the resulting TiO_2 phase allows for activation of H_2O *via* oxygen vacancies in close vicinity of the metallic Co^0 phase.^{66,67} Oxygen vacancies may be created by partial reduction of TiO_2 , *e.g.* by activation of CO over Co^0 together with surface oxygen of the TiO_2 phase in close vicinity forming CO_2 .⁶⁶ The vacancy formed may then activate H_2O replenishing the vacancy and forming either H_2 or surface hydroxyl species on the TiO_2 phase.^{66,68} The latter species have been reported to allow for a second bifunctional mechanism *via* the associative formate route.⁶⁶ At the periphery of metal particle and TiO_2 , adsorbed CO and surface hydroxyl species may form a formate intermediate resulting in the gaseous WGS products CO_2 and H_2 , while re-creating an oxygen vacancy. This vacancy may, once again, allow for H_2O activation. The potential activation of H_2O over reducible supports, such as CeO_2 , ZrO_2 , and TiO_2 , is the reason for extensive studies on superior bifunctional WGS catalysts using these carrier materials.^{58,67,69} In the present study, the formation of small cobaltous particles on the anatase particles may allow for such a bifunctional mechanism. However, the large cobalt particles, as identified by XRD and TEM-EDS, preclude an efficient use of precious Co^0 . Hence, the CoTiO_3 sample upon segregation represents an inferior WGS catalyst resulting in the low CO conversion observed (Figure II).

Regarding the FTS, the observed inactivity of the mixed-metal cobalt oxides phases towards the WGS reaction (Figure II) rises doubt over the previously proposed linkage between the presence of cobalt aluminate and an often reported increased CO_2 selectivity at increased CO conversion levels over $\text{Co}/\text{Al}_2\text{O}_3$ catalysts.^{4,5,7-9} The likely formation of both metal-support compounds under relevant conditions for the Co-based FTS was recently demonstrated by means of *in situ* XANES.^{13,15} Here, a contribution of formed cobalt aluminate towards WGS activity seems unlikely, which is in line with a recent study testing the performance of a $\text{Pt-Co}/\text{Al}_2\text{O}_3$ catalyst at CO conversions up to 97%.⁴ A reversible increase in the CO_2 selectivity was observed when comparing the catalyst's performance before and after exposure to such high FT conversion levels *via* cyclic adjustment of the space velocity, while cobalt aluminate species are expected to be irreducible at given conditions.⁴ Significant contributions of a CoTiO_3 phase, potentially forming during FTS over a Co/TiO_2 catalyst,¹⁵ to an increased CO_2 selectivity at high FT conversion levels is also unlikely given the catalytic results presented here. Literature on the CO_2 selectivity at high FT conversions catalysed by cobalt is generally scarce. Comparative studies on the FT performance over

Al₂O₃-, SiO₂-, and TiO₂-supported Co-based catalysts by Li *et al.* report a more pronounced increase of the CO₂ selectivity with conversion for the Al₂O₃ support than for TiO₂, while only a little increase was observed for the SiO₂ supported catalyst.^{5,6,70} However, the catalysts studied had different properties such as crystallite size and promoters preventing definite conclusions on the potential WGS activity of formed metal-support compounds, which are also expected to have different concentrations in the various catalysts.¹²

4. Summary and conclusions

The benzyl alcohol route was shown to enable the synthesis of amorphous mixed-metal cobalt oxides. However, an inhomogeneous atomic distribution was identified after transforming the samples to crystalline phases *via* calcination in air by combining a variety of complementary characterisation techniques, which is probably an artefact of the initial amorphous character and the slow atomic diffusion during calcination. No distinct WGS activity was observed for the cobalt aluminate spinel prepared in this study. In contrast, the cobalt titanate perovskite was shown to catalyse the WGS reaction after an extended activation period of 35-40 h at 325 °C. However, this mixed-metal cobalt oxide was shown to undergo full phase transformation *via* partial reduction forming anatase-TiO₂ and metallic Co, which is known to be WGS active in the studied temperature range. Hence, a previously suggested link between the formation of mixed-metal cobalt oxides in Co-based catalysts and an increased CO₂ selectivity at high conversion levels in the FTS could not be confirmed. Both mixed-metal oxides, the nano-particulate cobalt aluminate and cobalt titanate synthesised here, were shown to be WGS inactive for given feed gas composition and temperatures below 325 °C. Hence, an increased CO₂ formation during FTS at high conversion levels cannot be ascribed to the formation of such metal-support compounds.

Acknowledgements

Financial support from the DST-NRF Centre of Excellence in Catalysis (c*change), the UK Catalysis Hub, the University of Cape Town (UCT), the University College London (UCL), and the German Academic Exchange Service (DAAD) is gratefully acknowledged. Anna Petersen of the Catalysis Institute (UCT) and c*change is kindly acknowledged for the preparation of co-precipitated bulk-phased CoAl₂O₄. Sandeeran Govender (UCT) and Nicola Taccardi (University of Erlangen-Nuremberg) are thanked for the elemental analyses.

References

- 1 M. E. Dry and A. P. Steynberg, in *Fischer-Tropsch Technology*, eds. A. P. Steynberg

- and M. E. Dry, Elsevier, Amsterdam, 2004, vol. 152, pp. 406–481.
- 2 M. E. Dry, *Catal. Today*, 2002, **71**, 227–241.
- 3 M. E. Dry, in *Fischer-Tropsch Technology*, eds. A. P. Steynberg and M. E. Dry,
Elsevier, Amsterdam, 2004, vol. 152, pp. 196–257.
- 4 C. L. Tucker and E. van Steen, *Catal. Today*, In Press, DOI:
10.1016/j.cattod.2018.12.049.
- 5 J. Li, X. Zhan, Y. Zhang, G. Jacobs, T. Das and B. H. Davis, *Appl. Catal. A Gen.*, 2002,
228, 203–212.
- 6 J. Li, G. Jacobs, T. Das and B. H. Davis, *Appl. Catal. A Gen.*, 2002, **233**, 255–262.
- 7 W. Ma, G. Jacobs, Y. Ji, T. Bhatelia, D. B. Bukur, S. Khalid and B. H. Davis, *Top. Catal.*,
2011, **54**, 757–767.
- 8 D. B. Bukur, Z. Pan, W. Ma, G. Jacobs and B. H. Davis, *Catal. Letters*, 2012, **142**, 1382–
1387.
- 9 E. Rytter and A. Holmen, *ACS Catal.*, 2017, **7**, 5321–5328.
- 10 M. E. Dry, in *Fischer-Tropsch Technology*, eds. A. P. Steynberg and M. E. Dry,
Elsevier, Amsterdam, 2004, vol. 152, pp. 533–600.
- 11 P. J. van Berge, J. van de Loosdrecht, S. Barradas and A. M. van der Kraan, *Catal.*
Today, 2000, **58**, 321–334.
- 12 M. Wolf, H. Kotzé, N. Fischer and M. Claeys, *Faraday Discuss.*, 2017, **197**, 243–268.
- 13 N. E. Tsakoumis, J. C. Walmsley, M. Rønning, W. van Beek, E. Rytter and A. Holmen,
J. Am. Chem. Soc., 2017, **139**, 3706–3715.
- 14 M. Wolf, E. K. Gibson, E. J. Olivier, J. H. Neethling, C. R. A. Catlow, N. Fischer and M.
Claeys, *Catal. Today*, In Press, DOI: 10.1016/j.cattod.2019.01.065.
- 15 J. G. Moya-Cancino, A.-P. Honkanen, A. M. J. van der Eerden, H. Schaink, L.
Folkertsma, M. Ghiasi, A. Longo, F. M. F. de Groot, F. Meirer, S. Huotari and B. M.
Weckhuysen, *ChemCatChem*, 2019, **11**, 1–7.
- 16 N. Fischer, B. Clapham, T. Feltes, E. van Steen and M. Claeys, *Angew. Chemie Int.*
Ed., 2014, **53**, 1342–1345.
- 17 D. J. Moodley, A. M. Saib, J. van de Loosdrecht, C. A. Welker-Nieuwoudt, B. H.
Sigwebela and J. W. Niemantsverdriet, *Catal. Today*, 2011, **171**, 192–200.
- 18 M. Wolf, B. K. Mutuma, N. J. Coville, N. Fischer and M. Claeys, *ACS Catal.*, 2018, **8**,
3985–3989.
- 19 E. van Steen, M. Claeys, M. E. Dry, J. van de Loosdrecht, E. L. Viljoen and J. L.
Visagie, *J. Phys. Chem. B*, 2005, **109**, 3575–3577.
- 20 M. Karmaoui, N. J. O. Silva, V. S. Amaral, A. Ibarra, Á. Millán and F. Palacio,
Nanoscale, 2013, **5**, 4277–4283.
- 21 N. Shi, W. Cheng, H. Zhou, T. Fan and M. Niederberger, *Chem. Commun.*, 2015, **51**,
1338–1340.
- 22 M. Wolf, N. Fischer and M. Claeys, *Mater. Chem. Phys.*, 2018, **213**, 305–312.
- 23 M. Niederberger and G. Garnweitner, *Chem. - A Eur. J.*, 2006, **12**, 7282–7302.
- 24 ICDD, *PDF-2 Release 2008 (Database)*, International Centre for Diffraction Data,
Newtown Square, USA, 2008.
- 25 A. A. Coelho, *J. Appl. Crystallogr.*, 2003, **36**, 86–95.
- 26 P. Scherrer, *Nachrichten von der Gesellschaft der Wissenschaften zu Göttingen*,
Math. Klasse, 1918, 98–100.
- 27 G. Bergeret and P. Gallezot, in *Handbook of Heterogeneous Catalysis*, eds. G. Ertl, H.
Knözinger, F. Schüth and J. Weitkamp, Wiley-VCH, Weinheim, Germany, 2nd edn.,

- 2008, pp. 738–765.
- 28 MATLAB Release R2015b, The MathWorks, Inc., Natick, United States, 2015.
- 29 T. C. O’Haver, *Command line peak fitter for time series signals*,
<https://www.mathworks.com/matlabcentral/fileexchange/23611-command-line-peak-fitter-for-time-series-signals-version-8-1-july-2016>, 8.1., 2015.
- 30 A. J. Dent, G. Cibin, S. Ramos, A. D. Smith, S. M. Scott, L. Varandas, M. R. Pearson, N. A. Krumpa, C. P. Jones and P. E. Robbins, *J. Phys. Conf. Ser.*, 2009, **190**, 012039.
- 31 B. Ravel and M. Newville, *J. Synchrotron Radiat.*, 2005, **12**, 537–541.
- 32 M. Newville, *J. Synchrotron Radiat.*, 2001, **8**, 322–324.
- 33 N. T. J. Luchters, J. V. Fletcher, S. J. Roberts and J. C. Q. Fletcher, *Bull. Chem. React. Eng. Catal.*, 2017, **12**, 106–112.
- 34 T. Mimani and S. Ghosh, *Curr. Sci.*, 2000, **78**, 892–896.
- 35 J. Zou and W. Zheng, *Ceram. Int.*, 2016, **42**, 8198–8205.
- 36 X. Liu and C. T. Prewitt, *Phys. Chem. Miner.*, 1990, **17**, 168–172.
- 37 H. S. C. O’Neill, *Eur. J. Mineral.*, 1994, **6**, 603–609.
- 38 E. Mwenesongole, Ph.D. thesis, University of Pretoria, 2008.
- 39 J. Merikhi, H.-O. Jungk and C. Feldmann, *J. Mater. Chem.*, 2000, **10**, 1311–1314.
- 40 M. Zayat and D. Levy, *Chem. Mater.*, 2000, **12**, 2763–2769.
- 41 W. Li, J. Li and J. Guo, *J. Eur. Ceram. Soc.*, 2003, **23**, 2289–2295.
- 42 R. W. G. Wyckoff, *The Structure of Crystals*, Reinhold Publishing Corporation, New York, 2nd edn., 1935.
- 43 J. Zuo, C. Xu, Y. Liu and Y. Quian, *Nanostructured Mater.*, 1998, **10**, 1331–1335.
- 44 B. Jongsomjit, J. Panpranot and J. G. Goodwin Jr., *J. Catal.*, 2001, **204**, 98–109.
- 45 M. Shilpy, M. A. Ehsan, T. H. Ali, S. B. A. Hamid and M. E. Ali, *RSC Adv.*, 2015, **5**, 79644–79653.
- 46 M. A. Ehsan, R. Naeem, H. Khaledi, M. Sohail, A. H. Saeed and M. Mazhar, *Dalt. Trans.*, 2016, **45**, 10222–10232.
- 47 F. Casadio, A. Bezúr, I. Fiedler, K. Muir, T. Trad and S. MacCagnola, *J. Raman Spectrosc.*, 2012, **43**, 1761–1771.
- 48 E. van Steen, G. S. Sewell, R. A. Makhothe, C. Micklethwaite, H. Manstein, M. de Lange and C. T. O’Connor, *J. Catal.*, 1996, **162**, 220–229.
- 49 J. H. Hwang, E. N. Son, R. Lee, S. H. Kim, J. I. Baek, H. J. Ryu, K. T. Lee and J. M. Sohn, *Catal. Today*, 2018, **303**, 13–18.
- 50 A. Moen, D. G. Nicholson, B. S. Clausen, P. L. Hansen, A. Molenbroek and G. Steffensen, *Chem. Mater.*, 1997, **9**, 1241–1247.
- 51 G. Jacobs, T. K. Das, P. M. Patterson, J. Li, L. Sanchez and B. H. Davis, *Appl. Catal. A Gen.*, 2003, **247**, 335–343.
- 52 F. Farges, G. Brown and J. Rehr, *Phys. Rev. B*, 1997, **56**, 1809–1819.
- 53 W. Bungmek, P. Viravathana, S. Prangsri-aroon, S. Chotiwan, O. Deutschmann and H. Schulz, *Proc. Int. Conf. Environ. Ind. Innov.*, 2011, **12**, 65–69.
- 54 C. Li, X. Han, F. Cheng, Y. Hu, C. Chen and J. Chen, *Nat. Commun.*, 2015, **6**, 7345.
- 55 A. Kuzmin and J. Chaboy, *IUCrJ*, 2014, **1**, 571–589.
- 56 B. Ernst, A. Bensaddik, L. Hilaire, P. Chaumette and A. Kiennemann, *Catal. Today*, 1998, **39**, 329–341.
- 57 G. Cheng, J. D. Carter and T. Guo, *Chem. Phys. Lett.*, 2004, **400**, 122–127.
- 58 C. Ratnasamy and J. P. Wagner, *Catal. Rev.*, 2009, **51**, 325–440.
- 59 M. Wolf, N. Fischer and M. Claeys, *Catal. Today*, 2016, **275**, 135–140.

- 60 N. Tien-Thao, H. Alamdari, M. H. Zahedi-Niaki and S. Kaliaguine, *Appl. Catal. A Gen.*, 2006, **311**, 204–212.
- 61 L. Bedel, A. C. Roger, C. Estournes and A. Kiennemann, *Catal. Today*, 2003, **85**, 207–218.
- 62 L. Adijanto, V. B. Padmanabhan, K. Rainer, R. J. Gorte and J. M. Vohs, *J. Mater. Chem.*, 2012, **22**, 11396–11402.
- 63 D. Neagu, T.-S. Oh, D. N. Miller, H. Ménard, S. M. Bukhari, S. R. Gamble, R. J. Gorte, J. M. Vohs and J. T. S. Irvine, *Nat. Commun.*, 2015, **6**, 8120.
- 64 O. Kwon, S. Sengodan, K. Kim, G. Kim, H. Y. Jeong, J. Shin, Y.-W. Ju, J. W. Han and G. Kim, *Nat. Commun.*, 2017, **8**, 15967.
- 65 D. Neagu, E. I. Papaioannou, W. K. W. Ramli, D. N. Miller, B. J. Murdoch, H. Ménard, A. Umar, A. J. Barlow, P. J. Cumpson, J. T. S. Irvine and I. S. Metcalfe, *Nat. Commun.*, 2017, **8**, 1855.
- 66 K. G. Azzam, I. V. Babich, K. Seshan and L. Lefferts, *J. Catal.*, 2007, **251**, 153–162.
- 67 D. C. Grenoble, M. M. Estadt and D. F. Ollis, *J. Catal.*, 1981, **67**, 90–102.
- 68 A. Hussain, J. Gracia, B. E. Nieuwenhuys and J. W. Niemantsverdriet, *ChemCatChem*, 2013, **5**, 2479–2488.
- 69 O. Thinon, F. Diehl, P. Avenier and Y. Schuurman, *Catal. Today*, 2008, **137**, 29–35.
- 70 J. Li, G. Jacobs, T. Das, Y. Zhang and B. Davis, *Appl. Catal. A Gen.*, 2002, **236**, 67–76.